Formation of Micrometer-Sized Textured Hexagonal Silicon Crystals via Nanoindentation

Mouad Bikerouin, Anna Marzegalli, Davide Spirito, Gerald J. K. Schaffar, Corrado Bongiorno, Fabrizio Rovaris, Mohamed Zaghloul, Agnieszka Anna Corley-Wiciak, Leo Miglio, Verena Maier-Kiener, Giovanni Capellini,* Antonio Massimiliano Mio, and Emilio Scalise*

A comprehensive study on the formation of micrometer-sized, textured hexagonal diamond silicon (hd-Si) crystals via nanoindentation followed by annealing is presented. Utilizing advanced characterization techniques such as polarized Raman spectroscopy, high-resolution transmission electron microscopy, and electron energy-loss spectroscopy, the successful transformation of silicon into high-quality hd-Si is demonstrated. The experimental results are further supported by first-principles calculations and molecular dynamics simulations. Notably, the hd-Si phase consists of nanometer-sized grains with slight misorientations, organized into large micrometer-scale textured domains. These findings underscore the potential of nanoindentation as a precise and versatile tool for inducing pressure-driven phase transformations, particularly for the stabilization of hexagonal silicon. The textured nature of hd-Si also presents a unique opportunity to tailor its optical properties, opening new avenues for its application in semiconductor and optoelectronic devices.

1. Introduction

Silicon (Si), one of the most abundant and globally distributed elements, is the foundational material for complementary metal oxide semiconductor (CMOS) technology, which powers Si-based microelectronics. Within this technology, Si is primarily utilized in its diamond cubic (dc) lattice form, which can be strained under certain conditions. Nevertheless, other Si allotropes offer intriguing potential for addressing the ever-growing demand for enhanced efficiency in data processing and transmission. Many of these Si polymorphs possess unique properties, positioning them as potential low-cost and monolithically integrable solutions. For instance, some Si crystal structures are promising for on-chip energy harvesting devices due to the low thermal conductivity and high thermoelectric efficiency.[1–4] Other silicon polymorphs also demonstrate high carrier mobility[5,6] and superconductivity,[7] which could pave the way for innovative electronic and hybrid devices.

Furthermore, some polymorphs have been predicted to exhibit a direct bandgap, enhancing light emission and detection capabilities for use in on-chip photonic circuits.[8–16] Among these, hexagonal diamond (hd or Si-IV) stands out as particularly appealing and its realization has been demonstrated in nanowires[17,18] and through advanced deposition techniques.[19] Notably, recent studies have showcased efficient light emission from hexagonal SiGe alloy nanowires, wherein the $2H\text{-}Si_{1-x}Ge_x$ exhibits a direct bandgap that can be continuously tuned over a broad range via composition engineering.[20,21] The emission yield of these alloys is comparable to that of direct-bandgap III–V

M. Bikerouin, A. Marzegalli, F. Rovaris, L. Miglio, E. Scalise
Department of Materials Science
University of Milano-Bicocca
Via R. Cozzi 55, I-20125 Milano, Italy
E-mail: emilio.scalise@unimib.it

D. Spirito, A. A. Corley-Wiciak, G. Capellini
IHP-Leibniz-Institut für innovative Mikroelektronik
Im Technologiepark 25, 15236 Frankfurt (Oder), Germany
E-mail: capellini@ihp-microelectronics.com

The ORCID identification number(s) for the author(s) of this article can be found under https://doi.org/10.1002/sstr.202400552.

D. Spirito
BCMaterials
Basque Center for Materials, Applications and Nanostructures
UPV/EHU Science Park, 48940 Leioa, Spain

G. J. K. Schaffar, V. Maier-Kiener
Department of Materials Science
Montanuniversität Leoben
Roseggerstrasse 12, 8700 Leoben, Austria

C. Bongiorno, M. Zaghloul, A. M. Mio
Institute for Microelectronics and Microsystems (IMM)
Consiglio Nazionale delle Ricerche (CNR)
Strada VIII N. 5, 95121 Catania, Italy

G. Capellini
Department of Sciences
Università Roma Tre
V.le G. Marconi 446, 00146 Rome, Italy

semiconductors, highlighting their potential for optoelectronic applications.[22–25] Nevertheless, synthesizing such hexagonal SiGe alloys has proven challenging, as it often requires the use of GaAs core nanowires as a growth template. This limitation underscores the necessity for novel synthesis methods that can directly grow high-quality, direct-bandgap SiGe alloys on silicon substrates.

In principle, hd-Si could serve as a template for the epitaxial growth of hexagonal SiGe alloys, given its pronounced thermal stability, which allows it to maintain structural integrity at temperatures exceeding 700 °C.[26] This makes hd-Si ideal for epitaxy and postprocessing in device fabrication. However, synthesizing uniform, high-quality hd-Si crystals remains a significant challenge. One promising method to access metastable silicon phases, including hd-Si, is nanoindentation, a high-pressure technique that has been effective in exploring the complex phase landscape of silicon, enabling the formation of several metastable phases not typically observed at ambient pressure. Under mechanical pressure, dc silicon (dc-Si) transitions into a metallic β-Sn phase (Si-II) at elevated pressures.[27,28] Upon pressure release, various metastable phases can emerge, depending on the specific experimental conditions. These include the body-centered-cubic phase bc8 (Si-III), rhombohedral r8 (Si-XII), two simple tetragonal phases, Si-VIII and Si-IX, as well as Si-XIII, which has an as-yet unidentified crystal structure.[26,29,30] Additionally, these metastable phases can undergo further transformations upon annealing.[31–35]

By combining nanoindentation with subsequent annealing, it becomes possible to induce phase transformations from the stable dc phase into hexagonal diamond silicon,[26,36] offering a controlled and scalable approach to hd-Si synthesis. However, the rational design of pressure-induced phase transformations aimed at the specific synthesis of the hd-Si phase remains largely unexplored. A deeper understanding of the mechanisms governing these phase transformations, along with the ability to precisely control these processes, is essential to fully harness the potential of hd-Si for industrial applications. Successfully integrating hd-Si into silicon-based devices using existing fabrication technologies would represent a substantial technological leap, with far-reaching applications in electronics and photonics.

In this article, we demonstrate the successful realization of high-quality, micrometer-sized, uniform, and textured hexagonal silicon through nanoindentation and subsequent annealing. This is comprehensively demonstrated by combining state-of-the-art characterization techniques, including polarized Raman spectroscopy, high-resolution transmission electron microscopy (TEM), and electron energy-loss spectroscopy (EELS). This achievement represents a significant advancement, as it provides a scalable and practical approach to synthesizing hd-Si with properties suitable for industrial applications. These experimental findings are further supported by first-principles calculations and molecular dynamics (MD) simulations utilizing machine learning (ML)-based interatomic potentials, offering robust insights into the factors driving hd-Si formation and stability. Our approach uniquely integrates experimental and computational methods to bridge the gap between the understanding of stress-induced phase transitions and their practical realization. This synergy enables us to identify critical parameters, such as

stress and annealing conditions, that govern the formation of high-quality hd-Si. Furthermore, the textured nature of hd-Si opens up new opportunities to tailor its optical and electronic properties, paving the way for innovative applications in photonics, energy harvesting, and high-mobility electronic devices.

2. Results and Discussion

Nanoindentation experiments were performed on monocrystalline silicon (001) using spherical indenters with varying radii and different sets of maximum loads. Following indentation, the samples were annealed in a furnace at 250 °C. The optical micrograph in **Figure 1**a shows the surface imprints produced by a 20 μm indenter tip under a maximum load of 665 mN. Three samples, each containing nine indentation pits, were prepared under identical conditions, with the detailed analysis below focusing on one representative sample. A magnified view of a single pit, acquired via scanning electron microscopy (SEM), is shown in Figure 1b. Additionally, Figure 1c,d displays scanning TEM (STEM) images of a cross-sectional cut from the same pit, revealing microstructural details of the transformed phases. It is worth noting that the geometry of the indenter strongly influences the pressure distribution and concentration beneath the contact, thereby affecting both the onset pressure for phase transformation and the potential for crack formation. Sharp indenters, such as the Berkovich type, generate higher local pressures and more abrupt stress gradients, which may increase the risk of cracking. In contrast, spherical tips distribute the load over a larger contact area, reducing peak stresses but requiring higher total loads to reach transformation pressures. The indenter geometry also determines the spatial distribution of stress, creating two distinct "hot spots": one dominated by octahedral shear stress (favoring dislocation-based plasticity) and the other by hydrostatic pressure (promoting phase transformations).[37] The formation of hd-Si depends critically on which of these mechanisms is activated first. Furthermore, a slower loading and unloading rate may facilitate the formation of stable intermediate phases that relax into hd-Si upon annealing, whereas rapid loading and unloading can lead to faster transitions into amorphous silicon (a-Si). Therefore, careful optimization of the indenter geometry and loading parameters is essential to guide the transformation pathways toward hd-Si formation while minimizing the risk of cracking. In our study, the choice of appropriate indentation parameters enabled the creation of a uniform phase transformation region with no visible cracks on the surface. Correspondingly, the load–displacement curves show no evidence of "pop-in" events during loading, indicating the absence of crystalline defect nucleation and propagation.

Out of the 27 total pits analyzed across three samples, 70% (eight out of nine pits in two samples, and five out of nine in the third) exhibited these desirable characteristics. In contrast, the remaining pits displayed signs of mechanical instability, with "pop-in" events observed in their loading curves. As further elucidated by the Raman spectroscopy results, the variation in pit morphology and mechanical response is directly linked to differences in the pressure-induced phase transformation behavior. In the majority of pits, silicon reached the critical pressure for
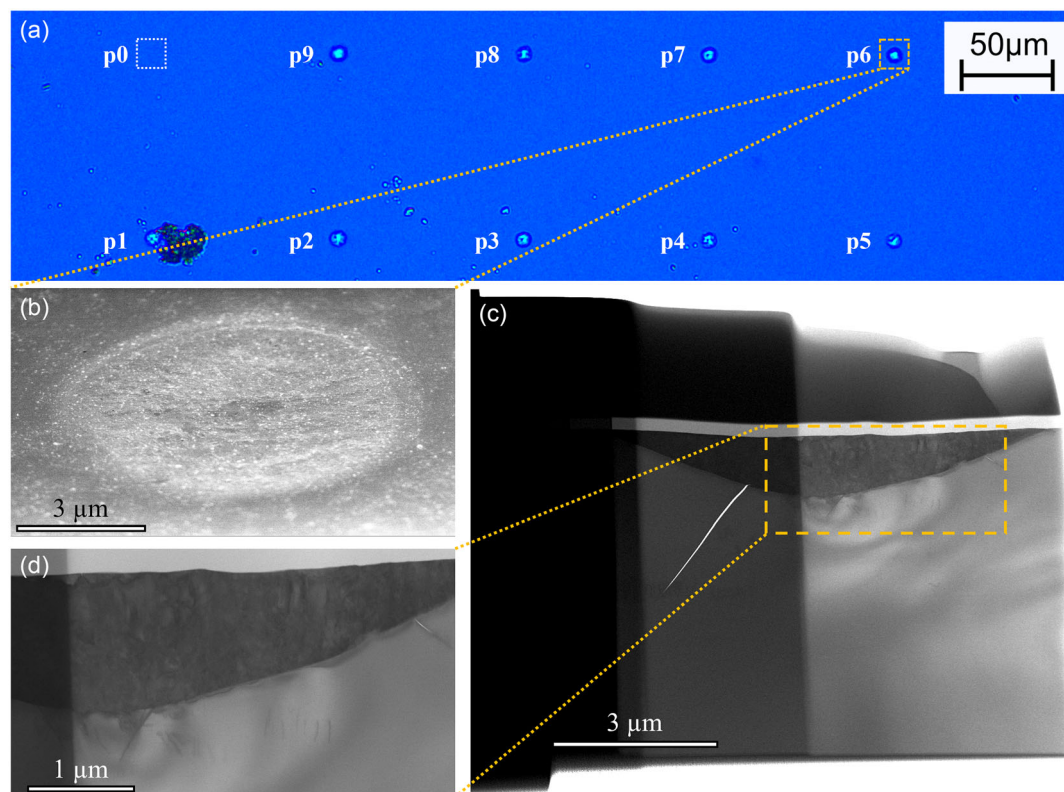
Figure 1. Characterization of silicon post-nanoindentation using a 20 µm spherical tip: a) optical micrograph of a series of silicon pits (p1–p9) formed by nanoindentation, with p0 represents the unindented, pristine dc-Si phase. b) SEM image of pit p6, highlighted by the yellow dashed box in (a), showing its surface topography. c) Low-magnification STEM bright-field image of the indented region at pit p6, illustrating the protective carbon layer deposited in situ via electron beam- and ion beam-induced deposition (EBID and IBID, respectively) and the underlying silicon phases. d) High-magnification STEM image of the localized region indicated in (c), revealing further details of the microstructural features within the transformed silicon phase.

phase transformation, resulting in a uniform, micrometer-sized transformed region. However, in the pits that exhibited "pop-in" events during loading, extensive plastic relaxation led to a higher density of defects and cracks, less uniform phase transformations, and smaller transformed regions. Additionally, the constraint-corrected contact stress during loading was derived from the continuously measured hardness using the constraint model of Hay et al.[38] as described in refs. [39,40]. The spherical indentation strain was calculated following the methodology outlined by Kalidindi and Pathak.[41,42] The resultant stress–strain curves, presented in the Supporting Information (Figure S4, Supporting Information), reveal a distinct elastic loading regime in all tests up to the transformation pressure. At pressures of 10–11 GPa, phase transformation begins, with the pressure stabilizing after its onset. Conversely, if cracking occurs, significant stress drops are observed. These stress drops correlate with pop-in events in the load–displacement signal, confirming the occurrence of cracking. The analysis of load–displacement and stress–strain curves provides a critical advantage: it enables the precise identification of the onset of phase transformation and cracking events. By leveraging this approach, future experiments can be meticulously designed to exceed the transformation threshold while remaining below the load levels that induce cracking.

To further investigate the structural changes induced by nanoindentation and annealing, we performed a detailed Raman spectroscopy analysis. In **Figure 2**, the nonpolarized Raman spectra of both as-indented and postannealed silicon are presented and compared with theoretical spectra derived from first-principles calculations. Before annealing, the experimental spectrum clearly reveals the presence of the bc8 and r8 silicon phases, with their corresponding Raman peak frequencies listed in **Table 1**. The crystal structures of these phases, along with their energy differences relative to the dc phase and their equilibrium volumes, calculated using density functional theory (DFT), are shown in panel (a). As can be revealed from Table 1, our experimental results are in good agreement with previously reported values in the literature. However, it is worth noting that Raman-active modes associated with the bc8 and r8 phases often display discrepancies across experimental reports. These variations can largely be attributed to the different pressure-inducing techniques employed, such as nanoindentation versus conventional compression experiments.[26,32,34,35,43–47] These techniques present several challenges, including limited experimental resolution, phase mixtures with overlapping features, and broadened peaks, which complicate the precise identification and assignment of Raman modes. Despite these challenges, our Raman spectra exhibit exceptional resolution compared to
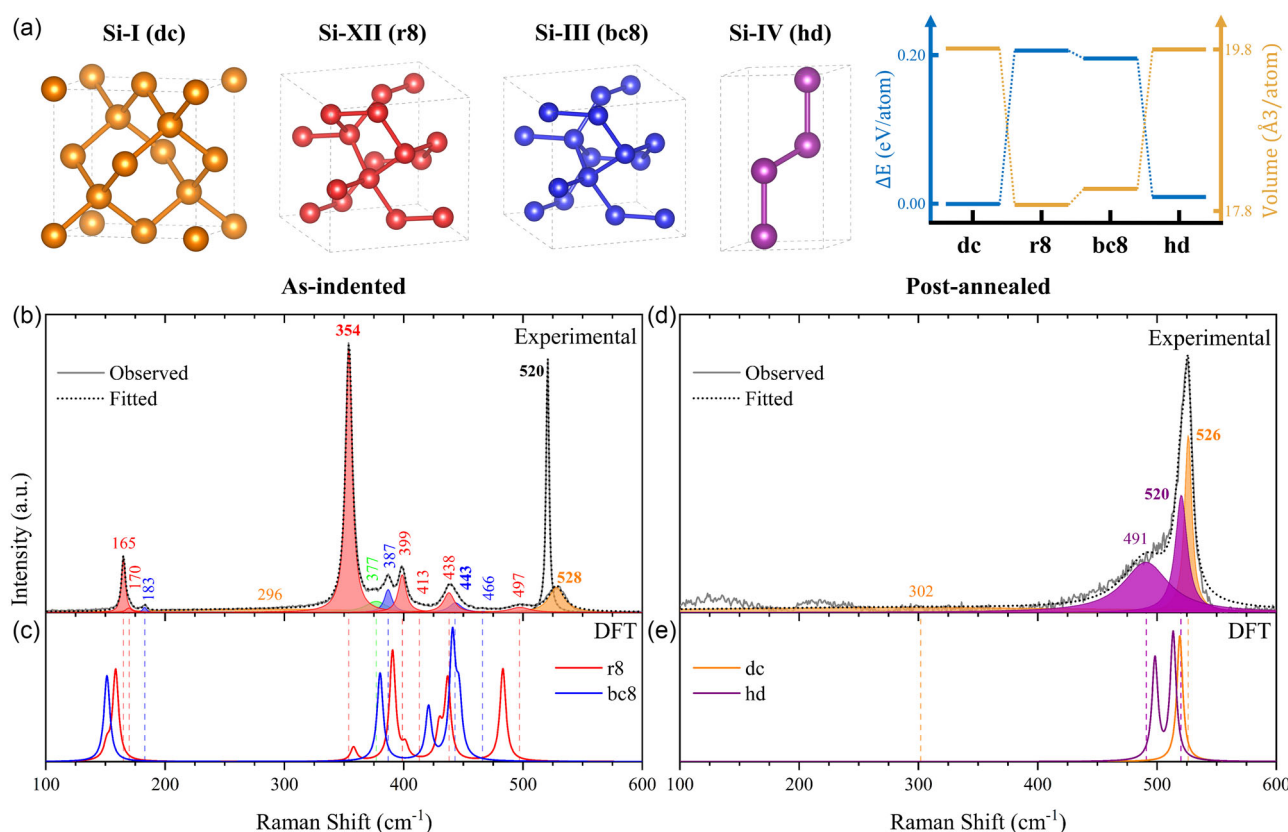
Figure 2. Structural and Raman spectroscopic analysis of silicon phases under nanoindentation and postannealing. a) Schematic representations of the silicon polymorphs observed in this study: Si-I (dc), Si-XII (r8), Si-III (bc8), and Si-IV (hd). The right plot illustrates the energy difference relative to the dc phase (ΔE in eV atom^{-1}) and the equilibrium volume (V in Å^3 atom^{-1}) at zero pressure for each polymorph, emphasizing their relative stabilities and structural similarities. Fitted nonpolarized experimental Raman spectra of 20 μm tip indented silicon: b) as-indented and d) postannealed. The fitting procedure used peak position, intensity, and width as free-fitting parameters. As a reference for the fitting, the frequencies of Raman-active modes for different metastable phases, as reported in previous experimental studies, were employed. Peaks corresponding to various metastable phases are represented by Lorentzian functions: dc (orange), hd (purple), r8 (red), and bc8 (blue). A distinct Raman peak at 377 cm^{-1}, indicative of a mixture of r8 and bc8 silicon phases, was identified. For comparison, the pristine Si spectrum is included in the graph. DFT computed Raman spectra are shown for c) r8 and bc8 and e) dc and hd. The theoretical spectra were generated using Lorentzian curves with a FWHM of 3 cm^{-1} to approximately reproduce the experimental FWHM of pristine Si. Experimentally extracted peak positions corresponding to various metastable phases are indicated with dashed lines.

previous studies, capturing all Raman-active phonon modes. This enhanced resolution enables clear identification of the r8 and bc8 phases. Table 1 includes the theoretical zone-center Raman-active modes for the r8 and bc8 phases. By focusing on the principal Raman peak frequencies most commonly reported in experiments for each phase, specifically 443.1 ± 3.4 cm^{-1} (T_g) for bc8 and 354.5 ± 0.5 cm^{-1} (A_g) for r8, we observe strong agreement with our DFT computations. These Raman modes are characteristic of the bc8 and r8 phases, clearly distinguish them from other possible phases. It is therefore evident that the as-transformed silicon is predominantly composed of the r8 and bc8 phases, with some residual dc-Si also present. For dc-Si, we computed the Raman-active T_{2g} mode, originating from a triply degenerate longitudinal optical (LO)–transverse optical (TO) phonon mode, yielding a 519.08 cm^{-1} value. This result closely matches the experimental value of 520.7 cm^{-1}, as measured in the pristine (unindented) region of the silicon sample (p0 in Figure 1a). For comparison, the corresponding spectrum is also shown in Figure 2b. Notably, the dc-Si peak

in the indented pits is shifted, indicating the presence of compressive strain in those regions. The conclusions drawn from the as-indented spectra are further supported by Figure S1, Supporting Information, where consistent peak positions were observed across different pits, reinforcing the reliability of our findings.

After annealing, significant changes in the Raman spectra are observed, particularly the disappearance of peaks associated with the bc8 and r8 phases and the emergence of new peaks corresponding to the hd phase, indicating complete structural transformations. Specifically, an asymmetric peak with a lower wave-number shoulder is observed around 520 cm^{-1}, which is best fitted by a composite of dc and hd phases. Once again, we find good qualitative agreement between the experimental Raman spectra and our DFT computations. All specific Raman peaks for the hd phase are listed in Table 1. The nondegenerate A_{1g} mode corresponds to the LO phonon mode, while the doubly degenerate E_{1g} and E_{2g} modes correspond to TO phonon modes. The Raman-active modes for the hd phase were theoretically

ADVANCED
SCIENCE NEWS
www.advancedsciencenews.com

small
structures
www.small-structures.com

Table 1. Comparison of experimental and theoretical Raman frequencies (in cm^{-1}) for various investigated silicon phases.

Phase[a]	Raman Mode	This work Exp.	This work Theo.	Exp.[88]	Exp.[32]	Exp.[43]	Exp.[87]	Exp.[19]	Exp.[48]
					Literature				
dc	T_{2g}	527.0 ± 3.2	519.08	520.3	516–524	522–539	–	–	521
hd	E_{2g}	487.2 ± 7.5	498.27	–	–	–	–	491.7–494.2	496
	E_{1g}	518.4 ± 6.2	513.38	–	–	–	–	506.9–513.8	514
	A_{1g}	518.4 ± 6.2	513.71	–	–	–	–	516.9–519.8	514
r8	A_g	165.2 ± 0.2	151.11	164.8	165.9 ± 1.1	162–164	165	–	–
	E_g	170.9 ± 0.9	158.53	170.0	–	169	170	–	–
	A_g	354.5 ± 0.5	357.93	351.9	353.9 ± 0.9	357	352	–	–
	E_g	375.6 ± 1.1	390.64	373.3	378 ± 0.9	–	373	–	–
	A_g	399.6 ± 0.5	401.34	397.1	398.5 ± 1.5	401	397	–	–
	A_g	415.8 ± 3.0	429.79	412	–	415	413	–	–
	E_g	436.9 ± 2.4	436.86	–	–	–	433	–	–
	E_g	495.1 ± 3.7	483.16	–	495.6	490	495	–	–
bc8	T_g	182.8 ± 0.4	151.24	182.4	184 ± 1.2	–	–	–	–
	T_g	375.6 ± 1.1	380.19	373.3	378 ± 0.9	–	–	–	–
	A_g	386.6 ± 0.7	420.80	384.2	386.1 ± 1.2	388–393	–	–	–
	T_g	443.1 ± 3.4	440.84	437.5	442.1 ± 1.1	443–447	–	–	–
	E_g	466.0 ± 4.3	446.28	463	–	–	–	–	–

[a]Phonon modes have been assigned on theoretical calculations. Previously reported experimental values are also included for reference. The standard deviation of the frequencies, derived from the analysis of multiple pits, represents the associated errors.

determined to be 498.27 cm^{-1} (E_{2g}), 513.39 cm^{-1} (E_{1g}), and 513.71 cm^{-1} (A_{1g}). These theoretical values closely align with previously reported experimental Raman frequencies for hd nanowires: 496 cm^{-1} (E_{2g}), 514 cm^{-1} (E_{1g}), and 514 cm^{-1} (A_{1g}).[48] In contrast, our current experimental data show a downshift of the E_{2g} mode and an upshift of the A_{1g} and E_{1g} modes, consistent with the presence of uniaxial strain. Notably, in both the theoretical and experimental data, the E_{1g} and A_{1g} modes occur at nearly identical frequencies and are unresolved. The width of the experimental hd-Si peak at 520 cm^{-1} is significantly narrower compared to previously reported hd-Si spectra,[19,26] indicating high crystal quality of the annealed samples. Additionally, no Raman peaks corresponding to a-Si were observed in either the as-indented or post-annealed conditions. Specifically, the characteristic a-Si peaks at $\approx$480 cm^{-1} (TO), 380 cm^{-1} (LO), 300 cm^{-1} (LA), and within the range of 80–200 cm^{-1} (TA) were absent.[49] These conclusions hold consistently across all synthesized pits, as demonstrated in Figure S1, Supporting Information, further validating the robustness of our results.

It is important to note that, even after annealing, the dc-Si peak in the Raman spectra remains shifted due to residual compressive strain. The dc peak in the spectra exhibits significantly narrower widths, higher intensities, and a more pronounced frequency shift in the pits that underwent plastic relaxation after indentation, corresponding to the 30% of pits previously identified with "pop-in" events in their loading curves. Henceforth, these are designated as Group-II pits. In contrast, the remaining 70% of pits, which did not show "pop-in" events during loading,

display broader dc peaks, lower intensities, and smaller frequency shifts. These pits are designated as Group-I (see Figure S2 and S3, Supporting Information, for comparative Raman spectra and Figure S4, Supporting Information, for the corresponding loading curves). After annealing, Group-II pits exhibit a distinct morphology, characterized by the presence of cracks and extended defects, particularly in the dc regions within the transformed zone, as revealed by STEM images in **Figure 3**. The formation of these cracks impedes the full transformation from the dc phase to the bc8/r8 phases, resulting in smaller transformed regions and highly stressed dc areas. As a consequence, this leads to a reduced volume of the hd phase after annealing. This effect is even more pronounced when a smaller tip (10 μm) is used, with nearly 100% of the pits exhibiting these typical Group-II characteristics, as shown in Figure S6, Supporting Information.

In contrast, after annealing, Group-I pits, which predominate in silicon samples indented with a 20 μm tip, exhibit large, uniform transformed zones that are free of cracks (see Figure 3a,b). Atomic force microscopy (AFM) images also reveal significant differences in the indentation imprint heights between the two groups, as shown in panels (e) and (f), further confirming elastic deformation in Group-I pits and plastic deformation in Group-II pits. Based on the comparison between these two pit families, we propose a distinct approach (detailed indentation parameters are provided in the Experimental Section) aimed at optimizing the statistical occurrence of pits with superior transformed regions. The Raman analysis presented above, along
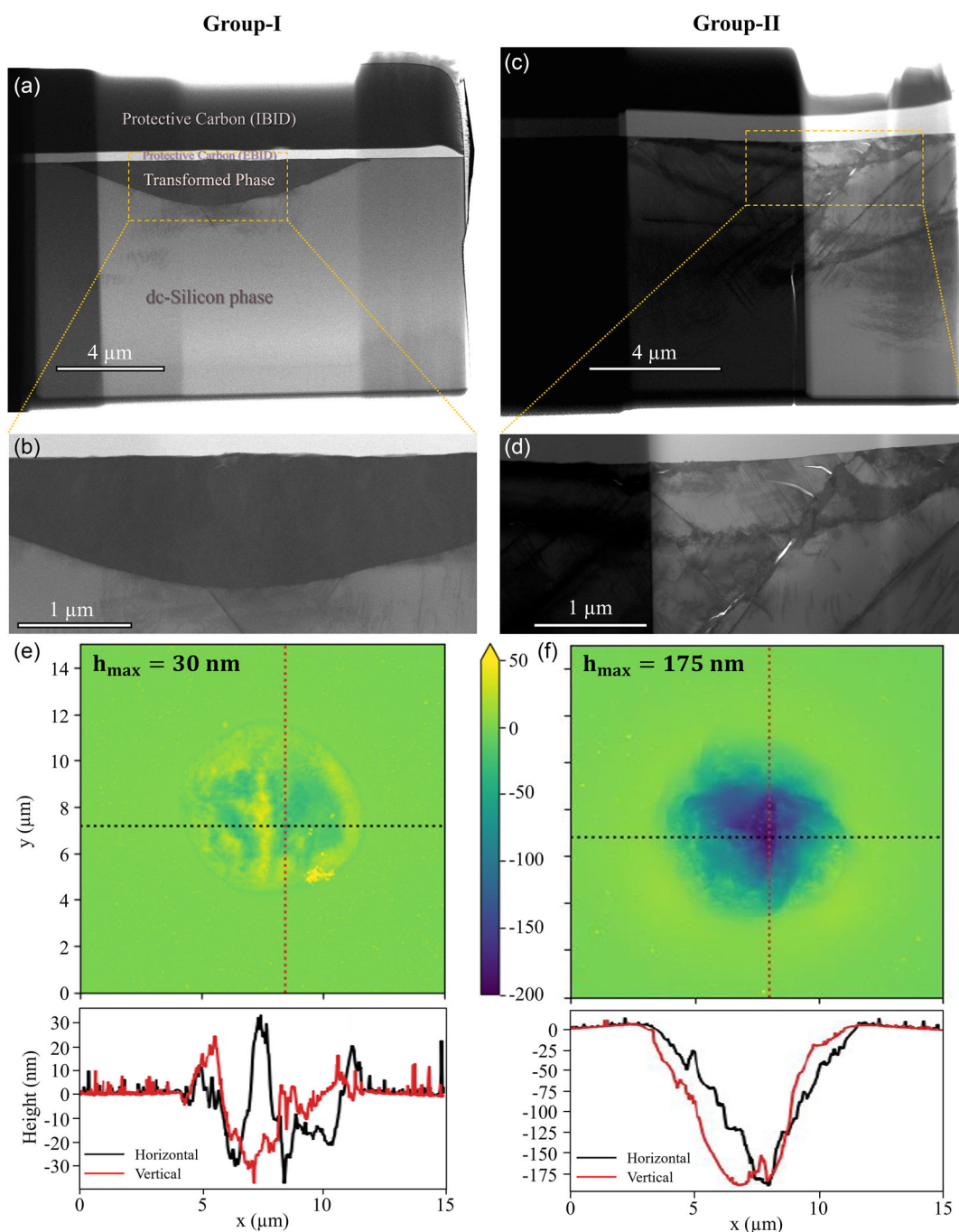
Figure 3. Low-magnification STEM bright-field images of postannealed silicon indented using a 20 μm tip, showcasing two distinct groups of pits: a,b) Group-I and c,d) Group-II. Each sample was protected by in situ deposited carbon layers (EBID and IBID) on the free surface before FIB preparation. Images (a,c) show overviews of the indented regions, while images (b,d) present higher magnification views of the areas enclosed by yellow dashed rectangles, focusing on the transformed silicon phases. Panels e,f) provide AFM topography maps and corresponding cross-sectional profiles for Group-I and Group-II, respectively, with the maximum height (h_{max}) indicated for each group. The cross-sectional profiles were taken across the deepest point of each pit to ensure accurate characterization of their topography.

with the forthcoming data, focuses primarily on Group-I pits due to their higher quality and statistical relevance for indentations performed with the 20 μm tip. Complementary data on Group-II pits can be found in the Supporting Information.

To further confirm the complete transformation of the bc8/r8 phases to the hd phase following annealing, the EELS analysis was performed. **Figure 4** presents a comparative analysis of experimental and theoretical low-loss EELS spectra for various
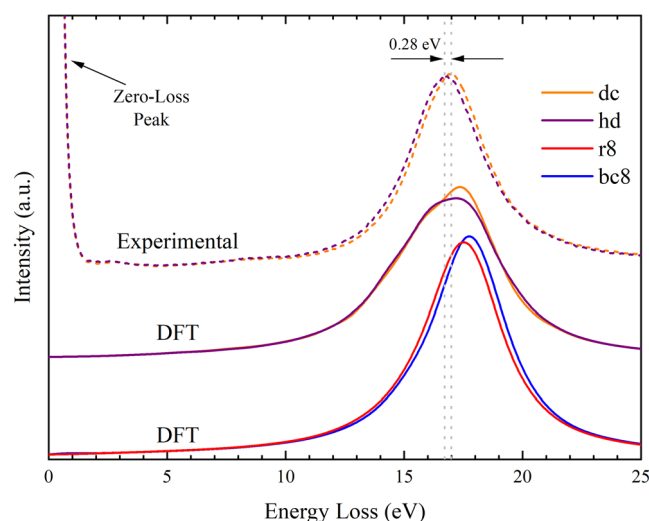
**ADVANCED
SCIENCE NEWS**

www.advancedsciencenews.com

**small
structures**

www.small-structures.com

Figure 4. Comparison of experimental and theoretical EELS of the low-loss region for postannealed indented silicon. The experimental spectra (dashed lines) are shown alongside the DFT calculations (solid lines) for the dc (orange), hd (purple), r8 (red), and bc8 (blue) silicon phases.

silicon phases. The key peak observed in the energy loss function corresponds to bulk plasmon excitations in the metastable silicon phases. Experimentally, this peak is observed at an energy of 17.0 eV for the dc phase, whereas the hd phase exhibits a redshift to 16.7 eV, highlighting phase-dependent optical properties. All the salient features observed in the experiment are correctly predicted through DFT computations, with the dc phase showing a peak at 17.36 eV and the hd phase at 17.21 eV. In contrast, the peaks associated with the r8 and bc8 phases are observed at higher energies, 17.52 and 17.76 eV, respectively, indicating a blueshift relative to the dc phase. The strong correlation between experimental results and theoretical predictions substantiates both methodologies, affirming the dependability of the techniques employed in this study while providing essential insights for distinguishing various silicon polymorphs. Furthermore, these findings can be exploited in future experimental studies to explore new silicon phases and their associated properties.

In order to conduct an in-depth analysis of the high-pressure metastable silicon phases both before and after annealing, and elucidate their crystallographic orientation, **Figure 5** presents the experimental and theoretical polarized Raman spectra as a function of the incidence polarization angle. In general, the visibility and intensity of specific Raman modes can be predicted using polarized Raman selection rules. These rules are dependent on the mode's symmetry and scattering geometry. The Raman intensity of a particular vibrational mode is proportional to the product of incident and scattered photon polarization vectors, as well as the Raman susceptibility tensor. According to group theory, the form of the Raman tensor, which includes the nonzero matrix elements, is determined by the point group and the structure's symmetry. However, the specific values of the matrix elements are determined by the electronic polarizability of the material system under investigation. The Raman tensors are typically presented in principal axis reference systems, but the direction of photon polarization is described in terms of the

sample's physical orientation. By examining the visibility and azimuthal dependence of the intensity of a Raman peak with respect to the polarization of the incident and scattered photons, it is possible to determine not only the crystal phase of a material but also its orientation. In our investigations, the analyzer is aligned with the incident polarization either at 0° (parallel polarization) or at 90° (perpendicular polarization). Both experiments and calculations for polarization-resolved Raman scattering were performed in the same back-scattering geometry. While the specific configurations of excitation and detection polarization do not influence the Raman shifts, they do affect the relative intensity of the Raman modes. The theoretical spectra as-indented (postannealed) are obtained by combining the contributions due to the r8 and bc8 (dc and hd) phases. The exceptional agreement between experimental and theoretical spectra reinforces the conclusions drawn above by the analysis of the nonpolarized Raman spectra: r8 and bc8 phases dominate the as-indented transformed phase, while after annealing only dc and hd-Si are detected. Especially for the r8 and bc8 phases, having different Raman modes compatible with other metastable phases, the analysis of the polarized Raman spectra shown in Figure 5 unambiguously evidences the formation of these two phases but excluding other possible metastable phases. Moreover, these two phases show coherence in their crystallographic orientation and their Raman signatures are always coupled, suggesting that the formed r8/bc8-Si is a crystalline mixture of the two phases appearing together,[50] but not two independent phases as can be formed in a diamond anvil cell (DAC).[51–54]

Additionally, the scattering intensities of the Raman-active modes predicted and measured before annealing (see Figure 5) are highest for polarization perpendicular to the indentation axis and lowest for parallel polarization, at 0° of incidence polarization angle, while it gets the contrary approaching 90° of incidence polarization angle. Thus, both phases have coherent dependence on the intensity of the Raman peaks with respect to the polarization of the incident and scattered photons. A similar behavior is observed for the spectra measured after annealing and compared to the simulations for hd and dc phases, suggesting a preferred crystallographic orientation of all metastable phases. This is confirmed in Figure S1, Supporting Information, where the same peak frequency, full width at half maximum (FWHM), and dependence on different polarization configurations were observed in other pits, indicating the common crystalline orientation of all metastable-Si structures formed in each pit, ruling out a polycrystalline nature. Indeed, all these metastable phases follow the selection rules predicted theoretically, asserting effective control and high reproducibility across different pits and samples in the nanoindentation process, which leads to the pressure-induced phase transition, as well as in the subsequent phase transformation upon annealing. Moreover, these results enable polarized Raman spectroscopy to be a valuable tool to easily and accurately distinguish the different metastable phases in Si. Similar conclusions about the presence of bc8, r8, hd, and dc phases, together with their crystallographic orientation, may be extended to the case of the 10 μm tip (see Figure S8, S9, Supporting Information), but the transformed zones are considerably smaller (nm scale) because the formation of defects and cracks inhibits the phase transformation over large (μm scale) and uniform area.
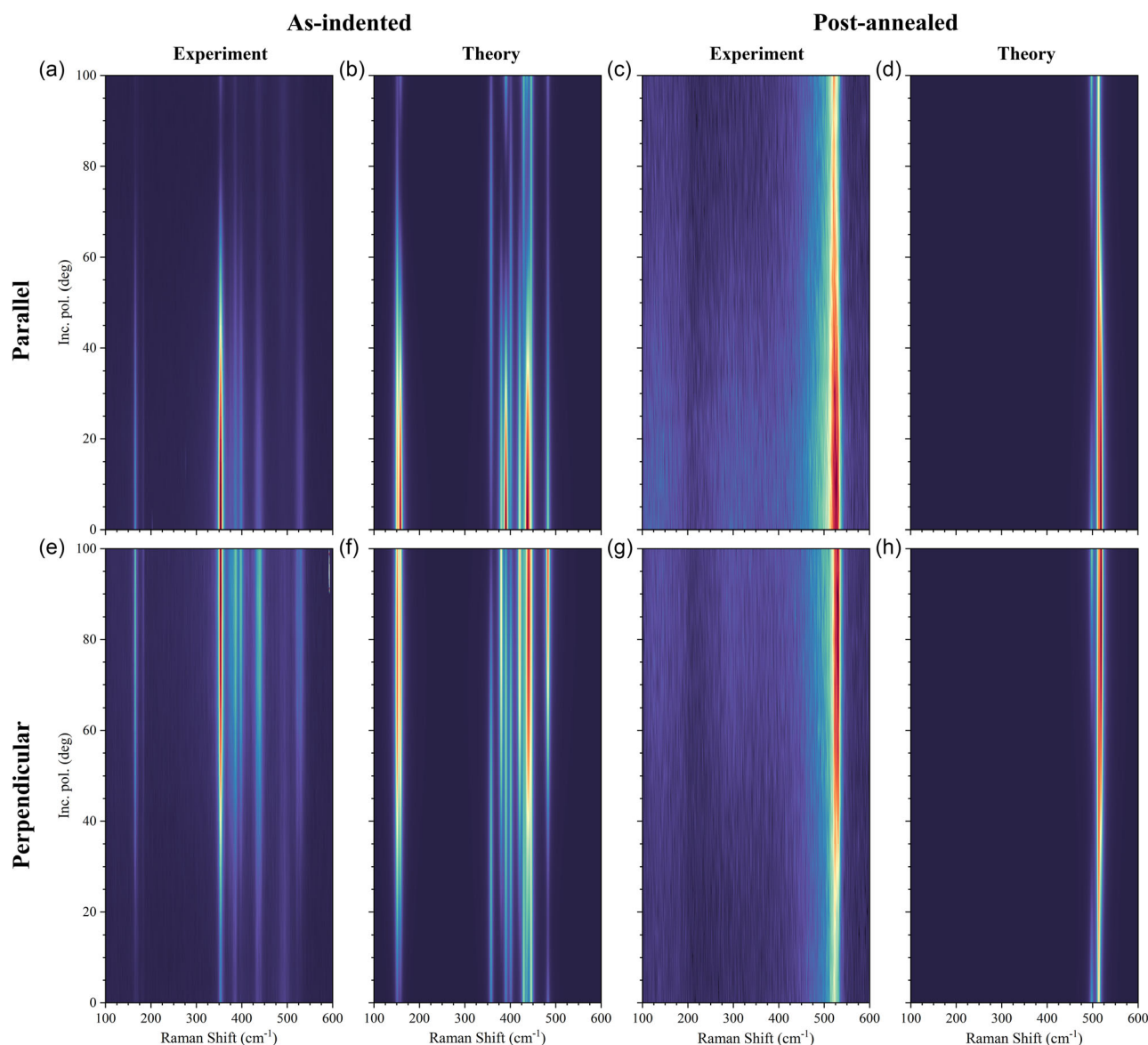
Figure 5. Raman spectra as a function of incidence polarization angle (α) for indented silicon before and after annealing. Panels a,c) show experimental results for as-indented and postannealed silicon in polarizer–analyzer parallel geometry, respectively. Panels e,g) display the corresponding experimental results in polarizer–analyzer perpendicular geometry. Panels b,d,f,h) illustrate the corresponding theoretical predictions. Panels b,f) include the combined theoretical results of the bc8 and r8 silicon phases, while panels d,h) represent the sum of DFT results for the hd and dc phases.

Summarizing the polarized and nonpolarized Raman results, we can conclude that the as-indented sample primarily consists of a bc8/r8 composite with high crystallographic coherence, except for some original dc phase with residual compressive stresses. Upon annealed, this bc8/r8 mixture transforms into an hd phase, possibly with some marginal recrystallization of dc-Si. Since the entire bc8/r8-Si phase mixture fully transforms into another phase after annealing, this suggests that r8/bc8-Si is a single hybrid phase rather than two distinct phases. This hypothesis is further supported by MD simulations exploiting a ML interatomic potential ,[55,56] which were employed to investigate the specific transition process from the bc8/r8 mixture to

the hd phase occurring during the annealing step. Details regarding the simulation setup and the analysis of the simulation output are detailed in the Section 5. The crystallographic structures of the four phases involved in the simulation are illustrated in Figure 2. Selected snapshots from the MD simulation are shown in **Figure 6**. The initial simulation cell, comprising 3456 atoms, was initialized with the bc8 crystal structure and thermalized for 20 ps at 750 K without any applied external pressure. During this thermalization step, a dynamical mixture of the bc8 and r8 phases is naturally formed, yielding a configuration similar to the first snapshot in Figure 6. Remarkably, it is not possible to recognize distinct nuclei of the two phases, but a
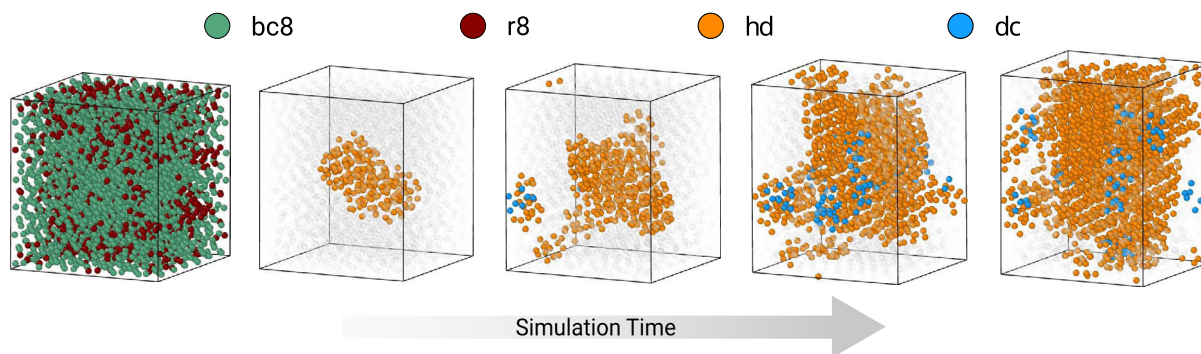
Figure 6. MD simulation leveraging an ML interatomic potential to illustrate the phase transformation from a mixture of bc8 (green) and r8 (wine) silicon phases to the hd (orange) phase. From the second snapshot onward, bc8/r8 phases are rendered transparent for clarity, allowing for better visualization of the hd phase. The dc phase is represented by blue atoms.

homogeneous mixture of the two phases appears after the thermalization at 750 K. This result suggests that it would be improbable to obtain distinct and large nuclei of bc8 and r8-Si at finite temperature and negligible residual stress, but a hybrid phase resulting from a mixture of the two phases.[57] Note that a temperature higher than room temperature has been used to speed up the thermalization in the MD simulations, but qualitatively similar results, except for a slight difference in the atomic percentage composition of bc8/r8, are expected for longer simulations using near-room temperatures and larger cells. Nevertheless, the atomistic mechanism of the formation of the bc8/r8 mixture can be inferred from such simulations and used to give predictive information about the process, like the relative percentage of bc8 and r8 in the mixture or the expected timescale of their transition to the hd phase. Further details about the atomistic mechanisms involved in the phase transition can be found in ref. [57], where we followed a similar approach. As shown in the second snapshots of Figure 6, a phase transition

from the bc8/r8 mixture to the hd phase can be identified during the simulation, with the formation of an initial nucleus. Successively, this initial nucleus of the hd phase grows and occupies almost completely the simulation cell, as can be observed in the latest snapshots of Figure 6. These snapshots also evidence how some of the starting bc8/r8 phase transforms back toward the most stable dc phase, as evidenced by some small nuclei of dc-Si in the simulation.

To further validate our previous conclusions and gain deeper insight into the microstructural characteristics of the hd-Si phase formed postannealing, we present the TEM analysis results in **Figure 7**. At first glance, the diffraction contrast image of the pit in cross-sectional view (Figure 7a) reveals relatively uniform contrast, with no visible grain boundaries or large domain contours. This uniformity suggests that the domain orientation in the modified area does not follow the random distribution typically seen in polycrystalline materials. Instead, it points to a preferential orientation within large domains, likely influenced
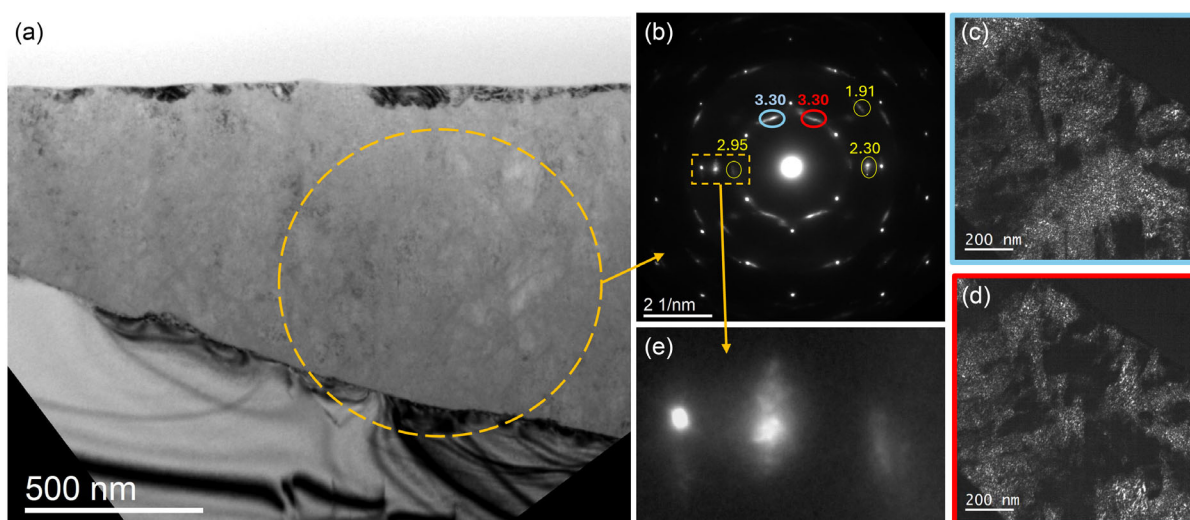

Figure 7. a) TEM micrograph of the pit in cross-view. b) Large SAED acquired at the pit center. Typical hd-Si reflections are highlighted. Brighter and ordered spots come from the silicon substrate. c,d) Dark field image acquired using the two arc-shaped spots at 3.30 Å in the same sample area. The images are complementary and cover almost all the sample region, demonstrating the presence of crystal texturing. e) Magnified view of some electron diffraction reflections, exhibiting a diffused and arc-shaped hd-Si spotty structure.

2400552 (9 of 14)

by the initial single-crystalline substrate. These findings align well with the polarized Raman results.

The large-area selective area electron diffraction (SAED) pattern acquired at the pit center, shown in Figure 7b, exhibits diffuse, arc-shaped contributions alongside the dc-Si substrate spots. All extracted plane distances from these signals are consistent with the hd-Si crystal structure but they are incompatible with standard dc-Si. This evidence supports the previous Raman and EELS measurements confirming the presence of hd-Si crystals and further indicates that nearly the entire pit displays diffraction spots corresponding to the hd phase. Meanwhile, the dc phase is confined to small, discontinuous regions ≈50 nm thick layer at the surface. The discrete and ordered angular distribution of these signals suggests a textured organization of the hd-Si crystals, as confirmed by the dark field images in Figure 7c,d. These images, obtained by selecting specific diffraction signals, highlight the areas of the sample contributing to those reflections. The bright regions in these images are complementary, covering almost the entire area, which suggests strong texture in the hd-Si crystal, forming macrodomains with a common orientation. However, the fragmented contrast within each macrodomain is clearly visible, indicating a nanostructured

material rather than large monocrystalline domains. This observation is corroborated by the very diffuse spots in the diffraction pattern (Figure 7e), which are typically associated with nanometer-sized grains. Therefore, macrodomain texturing alone does not provide a complete description of the system.

By tilting the sample and enhancing diffraction contrast using a smaller objective aperture, medium-sized domains within the macrodomains become evident, each showing fringed contrast, as shown in **Figure 8**a. Proper crystal alignment within these domains reveals clear zone-axis diffraction patterns in SAED, as illustrated in Figure 8b,c, which correspond well with the hd-Si crystal structure, as confirmed by simulations in Figure 8d,e. High-resolution micrographs reveal nanometer-sized grains within these medium-sized domains (Figure 8f), most of which share the same crystal orientation but exhibit slight misalignments. These misorientations, typically on the order of a few degrees, are enough to disrupt constructive interference between grains without introducing distinct diffraction spots beyond the average zone-axis. The combination of small grain size and slight misorientation produces highly diffuse, arc-shaped spots in diffraction, while the cumulative effect of these tilted grains generates a single, clean zone-axis. Many
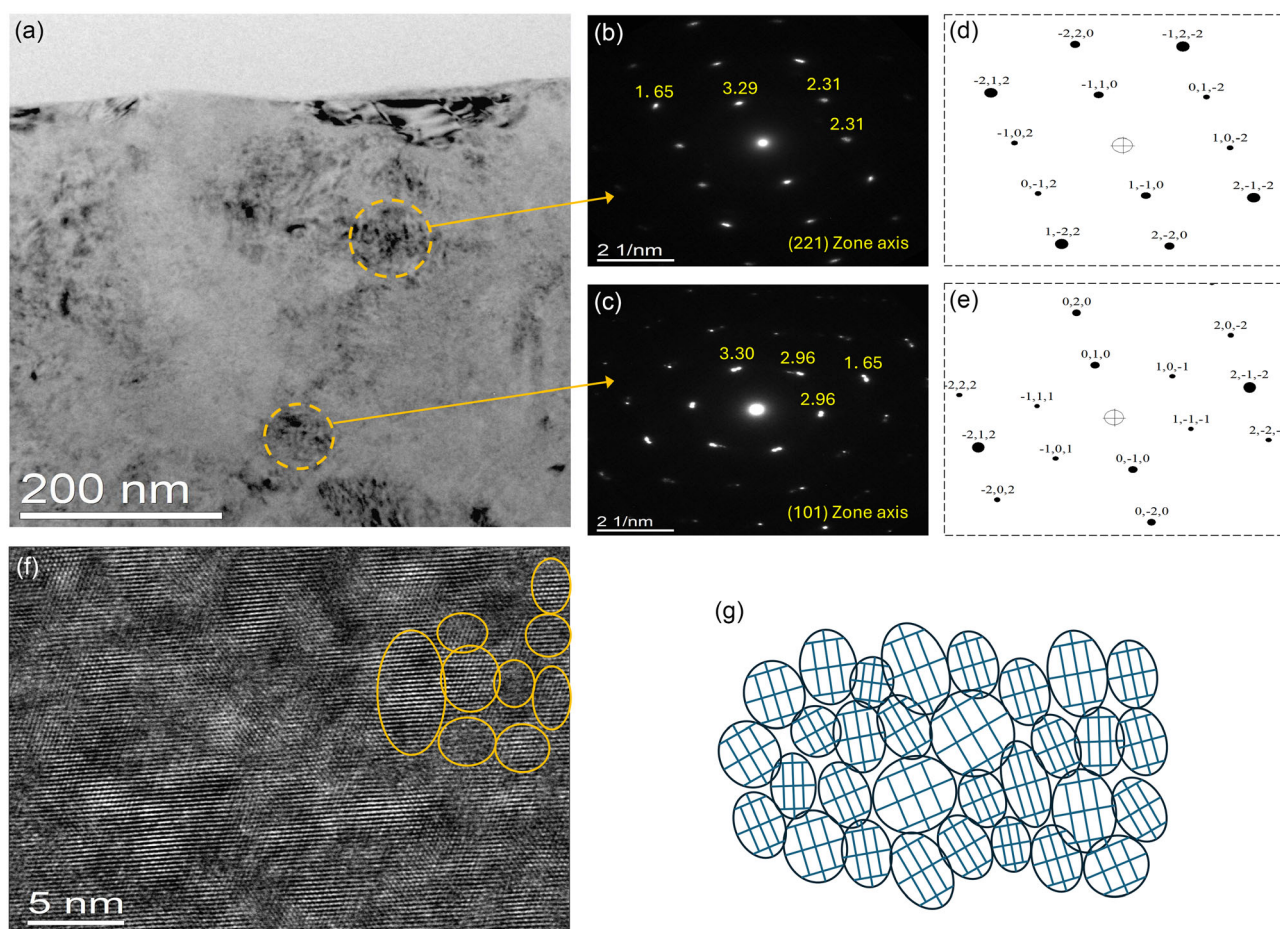

Figure 8. a) Cross-view TEM micrograph showing large crystal domains inside the pit. b,c) Diffraction patterns from the domains in the zone axes. d,e) Diffraction pattern simulations of the hd-Si zone axes. f) HR-TEM image of a single domain, composed of nanometer-sized crystals with similar orientation but slightly tilted each other. g) Schematic description of the crystal texture.

2400552 (10 of 14)

medium-sized domains likely share a common orientation, producing the macrodomain dark field images. The small grain size and misorientation naturally lead to a significant amount of distorted silicon structures, both within the textured nanocrystals and at the boundaries between these nanograins.

The TEM analysis clearly demonstrates the formation of large, micrometer-sized hexagonal silicon crystals beneath the indentations after annealing. However, it also reveals that the induced hd phase is neither monocrystalline nor polycrystalline. Instead, the hd-Si consists of textured nanocrystals organized into domains, which may exhibit slight misalignment (see Figure 8g). The presence of this texturing in both Group-I and Group-II pits, formed using a 20 μm spherical indenter, as well as in smaller 10 μm pits, suggests that this texture is likely an intrinsic feature of the pressure-induced and thermally driven phase transformation process.

Preferred crystallographic orientation has been observed in several high-pressure silicon phases, including β-Sn,[58] Imma,[59,60] and sh,[61] during pressure-induced deformation. Recently, similar findings have been extended to the bc8 phase, which forms under nonhydrostatic compression using a DAC.[62] In this case, bc8 crystals orient their <110> directions perpendicular to the compression axis while remaining free to rotate around this direction. The preferred orientation originates from the initial high pressure phase and it is transferred to successive daughter phases after unloading. In our experiment, the crystallographic texturing of the hd crystals (the daughter phase) may also result from the transformation pathway involving the bc8/r8 mixture (the parent phases). TEM analysis of the as-indented transformed phase confirms the presence of nanometer-sized, slightly misoriented grains, closely resembling those observed in the textured hd-Si after annealing.

3. Conclusion

In conclusion, our study not only provides new insights into the structural evolution of high-pressure silicon phases but demonstrates, for the first time, the successful formation of high-quality, micrometer-sized hexagonal silicon (hd-Si) crystals through nanoindentation. The hd-Si crystals exhibit remarkable uniformity and consistency across multiple indentation pits. The high quality of the hd-Si phase is evidenced by the presence of large and uniform transformed silicon domains, free from cracks and with minimal defects. In rare instances, defects and cracks within certain pits degraded the material quality, inhibiting the formation of large hd-Si domains. This comparative analysis of pits formed under varying nanoindentation conditions further provides critical insights into optimizing the indentation parameters necessary to achieve superior material quality. Specifically, the use of 20 μm spherical indenter with optimized nanoindentation parameters effectively distributes contact stress over a larger area, thereby reducing localized stress concentrations and minimizing the probability of cracking.

Notably, our findings further reveal that the hd-Si phase is not a monocrystalline structure, but rather a textured assembly of nanometer-sized grains with slight misorientations, an intrinsic feature of the pressure-induced and thermally driven phase transformation process. This texture introduces opportunities

to enhance the properties of hd-Si through the manipulation of anisotropy, strain, quantum confinement, and other novel effects, thereby expanding the possibilities for tailoring its properties to specific applications. Moreover, the textured hd-Si phase presents a promising platform for the epitaxial growth of hexagonal germanium (Ge) and SiGe alloys, which are particularly attractive for optoelectronic applications due to their direct bandgap properties, further broadening the scope of materials that can be integrated into future device technologies. Overall, this work highlights the versatility of nanoindentation as a precise tool for inducing controlled phase transformations in silicon and underscores the potential of hd-Si for future applications in semiconductor technology, optoelectronics, and advanced materials engineering.

4. Experimental Section

Nanoindentation: Indentation experiments were performed using a KLA Corporation (Milpitas, CA, USA) G200 System, equipped with spherical diamond tips of 10 and 20 μm radii, sourced from Synton-MDP (Nidau, Switzerland). The loading was performed at a constant strain rate of $\dot{\varepsilon} = 10^{-3}\,\text{s}^{-1}$, following the methodology outlined by Leitner et al.[40,63] The unloading was performed at a constant unloading rate of $\dot{P} = 1\,\text{mN}\,\text{s}^{-1}$. This slow unloading was performed to favor crystalline transformation rather than amorphization.[64–67] For indentations performed using the 20 μm radius tip, experiments were carried out up to the system's maximum applicable force ($P_{\text{max}} = 665\,\text{mN}$), ensuring sufficient force to trigger the expected phase transformations. In contrast, indentations with the 10 μm radius tip were conducted across three different maximum loads. One sample was subjected to the same maximal load as for the 20 μm tip ($P_{\text{max}} = 665\,\text{mN}$), while the other two samples were indented with reduced maximum loads of 570 and 425 mN, respectively. Despite the reduced force, the smaller tip applied larger local strains compared to the 20 μm indenter due to its geometry, leading to more pronounced mechanical responses. The most significant results obtained using the 10 μm indenter are presented in the supporting material, as the transformed phases generally exhibit lower quality compared to those produced with the 20 μm tip. The annealing was performed in quartz tube furnace under nitrogen atmosphere. The furnace was set at a temperature of 250 °C, and the sample was quickly inserted in it after the temperature was stabilized. The sample was annealed for 2 h. Then, it was extracted from the furnace and left to cool to room temperature in ambient atmosphere.

Raman Scattering Experiments: Raman spectroscopy was performed using a Renishaw inVia system, with an excitation laser wavelength of 532 nm in back-scattering geometry, with the laser incident along the sample crystalline direction [001] (z) of the substrate. The system is equipped with a polarizer for the excitation laser and an analyzer at the spectrometer's entrance. Additionally, an half-wave plate allows to rotate the polarization of the excitation by an angle α. Another half-wave plate allows to set the analyzer direction so that it can be parallel to α = 0, α = 0° or α = 90°. The sample is aligned so that the direction x' = [110] of the substrate is aligned with the direction α = 0°. It is important to note that the probing depth of the Raman laser in silicon is on the order of few hundreds of nanometers (500–600 at 532 nm). Therefore, Raman spectra predominantly probe near-surface regions. To confirm that hd-Si extends beyond this region, we employed cross-sectional TEM and SAED to characterize the material beneath the indented surface. These complementary techniques provide a more comprehensive picture of the transformed zone and confirm the presence of hd-Si beyond the Raman probing depth.

TEM, SAED, STEM, and EELS: Conventional TEM analyses in parallel beam and SAED were performed by using a JEOL JEM-2010F microscope, equipped with a Schottky field emission gun and operating at 200 keV. EELS was performed by using a JEOL ARM200F Cs-corrected microscope,

equipped with a cold-field emission gun and operating at 200 keV. A GIF Quantum ER system was used for EELS measurements. EELS spectra were acquired in spectrum imaging mode. TEM lamellae were prepared by focused ion beam (FIB) using a Thermofisher Helios 5 UC+ system, operating with 30 keV Ga+ and finally polishing at low energy (2 keV Ga+) to reduce residual FIB-induced amorphization. SEM and STEM have been performed by using the electron column of the same system.

5. Methods

MD Simulation: MD simulations have been performed with the LAMMPS code[68] exploiting the ML-based GAP potential.[55] The simulation shown in Figure 6 has been performed utilizing an integration step of 1 fs in the NPT ensemble with an initial equilibration step at zero pressure and 750 K for 20 ps. After this, a uniaxial tensile strain rate has been imposed in the vertical (z) direction as described in ref. [57]. The phase transition have been detected during the simulation exploiting a neural network-based phase recognition tool described in ref. [56] for the bc8 and r8 phases and a standard tool present in the OVITO software[69] and based on crystalline symmetry for the dc and the hd phases.

DFT Calculations: First-principles calculations within the DFT framework were performed using the Quantum Espresso code.[70] The exchange–correlation (XC) contribution to the total energy was modeled using the generalized gradient approximation with Perdew–Burke–Ernzerhof (PBE) parametrization.[71] We also employed the local density approximation (LDA),[72] strongly constrained and appropriately normed (SCAN)[73,74] assessed through the LIBXC library,[75] and PBE revised for solids (PBEsol)[76] functionals to benchmark against existing literature data. The electron–ion interaction was described using optimized norm-conserving Vanderbilt pseudopotentials[77] from the PseudoDojo set.[78] Wave functions were expressed using a plane-wave basis set with an energy cutoff of 100 Ry. Given the sensitivity of Raman intensities to reciprocal space sampling, a Γ-centered k-point mesh with a fine density of $0.05\,\text{Å}^{-1}$, according to the Monkhorst–Pack scheme, was used.[79] Structural geometry optimizations were performed via a variable cell relaxation procedure until the Hellmann–Feynman forces on each atom were less than $1\,\text{meV}\,\text{Å}^{-1}$ and the stress tensor components were below 0.02 kbar. The self-consistent field iteration convergence threshold was set to 10^{-10} eV. To evaluate the structural stability of the studied phases, phonon calculations were performed using density functional perturbation theory.[80] First-order resonant Raman spectra for various Porto configurations were computed with the QERAMAN code.[81] This calculation was undertaken to elucidate specific characteristics of the measured vibrational Raman spectra and to identify the metastable phases observed experimentally. The EELS curves were obtained using the Liouville–Lanczos approach to time-dependent DFT,[82] implemented in the turboEELS code.[83] To achieve convergence, we performed 6000 iterations in the Lanczos recursion and extrapolated the Lanczos coefficients to 100 000 iterations using the biconstant extrapolation method.[84] The EELS is obtained in the limit $q \rightarrow 0$, where q is the transferred momentum.

Relaxed structures were initially obtained by performing a full structural relaxation with respect to all degrees of freedom at zero pressure, utilizing various XC functionals. Subsequently, the isothermal bulk modulus (B_0) and its pressure derivative (B_0') were determined through a series of fixed-volume relaxations. The resulting energy-to-volume data were then fitted to the Vinet equation of state.[85] These results, summarized in Table S2, Supporting Information, were compared with both theoretical and experimental values available in the literature. However, it is important to acknowledge that experimental structural parameters are relatively scarce and, in some instances, derived from nanostructured or potentially strained samples. The differences in energy from the corresponding dc phase are also reported in Table S2, Supporting Information. Our findings indicate distinct trends in lattice parameters based on functional choice. Specifically, the LDA tends to overbind, while functionals incorporating gradient corrections, particularly the PBE functional, tend to underestimate the chemical bond strength. These tendencies are also reflected in the computed volumes and bulk modulus (B_0). Overall, results obtained

using the PBEsol and SCAN functionals exhibit better agreement with experimental data. Furthermore, our calculated structural properties are consistent with previous theoretical results, reinforcing the validity of our PBEsol and SCAN calculations as a reliable foundation for future experimental studies. On the other hand, the calculated energy differences within the SCAN functional are systematically larger than those from the PBE functional, which, in turn, are larger than those from the LDA and PBEsol. However, the energy differences between SCAN and the other XC functionals are quite small for the low-density tetrahedral polymorphs, with equilibrium volumes close to the dc phase, such as the hd phase. In contrast, for the high-density tetrahedral polymorphs, such as bc8 and r8 phases, there is a significant difference between the results obtained with different XC approximations. This reflects the similarity in bonding between dc and hd, and between r8 and bc8 phases. This also highlights the fact that predictions of phase stability are sensitive, in some cases strongly so, to the underlying treatment of XC effects.

The phonon band structures of the dc, hd, r8, and bc8 phases of silicon at zero pressure are plotted in Figure S10a–d. These plots demonstrate that all studied phases are dynamically stable at zero pressure, exhibiting no imaginary frequencies throughout the Brillouin zone. For the bc8 and r8 phases, the number of phonon branches is quadrupled compared to the dc phase due to the larger primitive cell, which enhances phonon scattering and reduces lattice thermal conductivity.[86] Additionally, the phonon spectra for the r8 phase qualitatively resemble those of the bc8 phase.

It should be noted that the consistency between our first-principles computations and experimental measurements of Raman-active mode frequencies across all studied silicon phases is due to a considered choice of the XC functional, as detailed in Table S3, Supporting Information. After a thorough analysis of the effects of the choice of XC functional and structural parameters, we adopted an approach where PBE XC functional is used in combination with the theoretically relaxed zero pressure structures obtained using the SCAN XC functional. However, the small discrepancies between the experimental and theoretical data can be attributed to the static (0 K) calculation and the harmonic approximation employed in the Raman calculations. Furthermore, Raman spectra were computed for structures relaxed at 0 GPa, but as demonstrated in the case of dc, the observed r8, bc8, and hd phases are likely under residual pressure. This residual pressure would lead to further shifts in peak positions and changes in the Raman intensities in the computed spectra. This phenomenon was also observed by Wong et al.[87] where bc8-Si and r8-Si phases recovered after indentation exhibited distorted unit cells, characterized by tensile strain along the indentation axis and compressive strain perpendicular to it. This strain leads to an overall reduction in unit cell volume equivalent to a quasihydrostatic compression of $\approx$4 GPa for the same phases recovered from DAC compression.[52] Furthermore, the crystals in the transformed zone are confirmed from TEM results to be 5–30 nm in size, implying that phonon confinement effects may shift Raman frequencies even further. Finally, Figure S11–S14, Supporting Information, show the atomic displacements of the Raman-active phonon modes, where the arrows indicate the vibration directions of atoms.

Supporting Information

Supporting Information is available from the Wiley Online Library or from the author.

Acknowledgements

**ADVANCED
SCIENCE NEWS**

www.advancedsciencenews.com

**small
structures**

www.small-structures.com

Conflict of Interest

The authors declare no conflict of interest.

Author Contributions

Mouad Bikerouin: data curation (lead); formal analysis (lead); investigation (equal); validation (equal); visualization (lead); writing—original draft (lead); writing—review and editing (equal). **Anna Marzegalli**: conceptualization (equal); formal analysis (equal); project administration (equal); validation (equal); writing—original draft (lead). **Davide Spirito**: formal analysis (equal); investigation (lead); writing—review and editing (equal). **Gerald J. K. Schaffar**: formal analysis (equal); investigation (equal); validation (equal); writing—review and editing (equal). **Corrado Bongiorno**: formal analysis (equal); investigation (equal); writing—review and editing (equal). **Fabrizio Rovaris**: investigation (equal); methodology (equal); validation (equal); writing—original draft (supporting); writing—review and editing (equal). **Mohamed Zaghloul**: investigation (supporting). **Agnieszka Anna Corley-Wiciak**: investigation (supporting); writing—review and editing (supporting). **Leo Miglio**: funding acquisition (supporting); resources (supporting); writing—review and editing (supporting). **Verena Maier-Kiener**: conceptualization (equal); resources (lead); supervision (lead); writing—review and editing (equal). **Giovanni Capellini**: conceptualization (lead); formal analysis (equal); resources (lead); supervision (lead); writing—review and editing (equal). **Antonio Massimiliano Mio**: conceptualization (equal); formal analysis (equal); funding acquisition (equal); investigation (equal); resources (lead); supervision (lead); writing—review and editing (equal). **Emilio Scalise**: conceptualization (lead); funding acquisition (lead); investigation (equal); resources (lead); supervision (lead); writing—original draft (equal); writing—review and editing (equal).

Data Availability Statement

The data that support the findings of this study are available from the corresponding author upon reasonable request.

Keywords

[1] P.-H. Du, J. Zhou, *Phys. B: Condens. Matter* **2021**, *618*, 413178.
[2] H. Shao, D. Ding, L. Zhang, C.-K. Dong, H. Zhang, *Mater. Today Phys.* **2022**, *27*, 100756.
[3] Z. Liu, N. Tan, C. Tang, *Eur. Phys. J. B* **2021**, *94*, 247.
[4] P. Zhang, T. Ouyang, C. Tang, C. He, J. Li, C. Zhang, M. Hu, J. Zhong, *Modell. Simul. Mater. Sci. Eng.* **2018**, *26*, 085006.
[5] Y. Guo, Q. Wang, Y. Kawazoe, P. Jena, *Sci. Rep.* **2015**, *5*, 14342.
[6] B. D. Malone, J. D. Sau, M. L. Cohen, *Phys. Rev. B* **2008**, *78*, 161202.
[7] B. D. Malone, J. D. Sau, M. L. Cohen, *Phys. Rev. B* **2008**, *78*, 035210.
[8] C. He, C. Zhang, J. Li, X. Peng, L. Meng, C. Tang, J. Zhong, *Phys. Chem. Chem. Phys.* **2016**, *18*, 9682.
[9] C.-P. Tang, J. Cao, S.-J. Xiong, *Phys. B: Condens. Matter* **2015**, *466*, 59.
[10] I.-H. Lee, Y. J. Oh, S. Kim, J. Lee, K. J. Chang, *Comput. Phys. Commun.* **2016**, *203*, 110.
[11] I.-H. Lee, J. Lee, Y. J. Oh, S. Kim, K. J. Chang, *Phys. Rev. B* **2014**, *90*, 115209.
[12] Q. Wang, B. Xu, J. Sun, H. Liu, Z. Zhao, D. Yu, C. Fan, J. He, *J. Am. Chem. Soc.* **2014**, *136*, 9826.
[13] H. J. Xiang, B. Huang, E. Kan, S.-H. Wei, X. G. Gong, *Phys. Rev. Lett.* **2013**, *110*, 118702.
[14] S. Botti, J. A. Flores-Livas, M. Amsler, S. Goedecker, M. A. L. Marques, *Phys. Rev. B* **2012**, *86*, 121204.
[15] M. L. Cohen, B. D. Malone, *J. Appl. Phys.* **2011**, *109*, 102402.
[16] V. A. Saleev, A. V. Shipilova, D. M. Proserpio, G. Fadda, *Eur. Phys. J. B* **2017**, *90*, 1.
[17] Z. He, J.-L. Maurice, Q. Li, D. Pribat, *Nanoscale* **2019**, *11*, 4846.
[18] J. Tang, J.-L. Maurice, F. Fossard, I. Florea, W. Chen, E. V. Johnson, M. Foldyna, L. Yu, P. Roca I Cabarrocas, *Nanoscale* **2017**, *9*, 8113.
[19] H. S. Ahn, S.-W. Kim, G. S. Lee, K. H. Kim, J. H. Lee, D. H. Ha, Y. T. Chun, S. Ryu, *Semicond. Sci. Technol.* **2021**, *36*, 095023.
[20] E. M. T. Fadaly, A. Dijkstra, J. R. Suckert, D. Ziss, M. A. J. Van Tilburg, C. Mao, Y. Ren, V. T. Van Lange, K. Korzun, S. Kölling, M. A. Verheijen, D. Busse, C. Rödl, J. Furthmüller, F. Bechstedt, J. Stangl, J. J. Finley, S. Botti, J. E. M. Haverkort, E. P. A. M. Bakkers, *Nature* **2020**, *580*, 205.
[21] W. H. J. Peeters, V. T. Van Lange, A. Belabbes, M. C. Van Hemert, M. M. Jansen, R. Farina, M. A. J. Van Tilburg, M. A. Verheijen, S. Botti, F. Bechstedt, J. E. M. Haverkort, E. P. A. M. Bakkers, *Nat. Commun.* **2024**, *15*, 5252.
[22] Z. Wang, Z. Zhang, S. Liu, J. Robertson, Y. Guo, *Appl. Phys. Lett.* **2021**, *118*, 172101.
[23] N. Bao, F. Guo, D. Kang, Y. Feng, H. Wang, J. Dai, *J. Appl. Phys.* **2021**, *129*, 145701.
[24] Q. Fan, W. Zhang, Y. Song, W. Zhang, S. Yun, *Semicond. Sci. Technol.* **2020**, *35*, 055012.
[25] Q. Fan, C. Chai, Q. Wei, K. Wong, Y. Liu, Y. Yang, *J. Mater. Sci.* **2018**, *53*, 2785.
[26] S. Wong, B. C. Johnson, B. Haberl, A. Mujica, J. C. Mccallum, J. S. Williams, J. E. Bradby, *J. Appl. Phys.* **2019**, *126*, 105901.
[27] M. C. Gupta, A. L. Ruoff, *J. Appl. Phys.* **1980**, *51*, 1072.
[28] J. Z. Hu, I. L. Spain, *Solid State Commun.* **1984**, *51*, 263.
[29] Z. Zhao, F. Tian, X. Dong, Q. Li, Q. Wang, H. Wang, X. Zhong, B. Xu, D. Yu, J. He, H.-T. Wang, Y. Ma, Y. Tian, *J. Am. Chem. Soc.* **2012**, *134*, 12362.
[30] A. Mujica, C. J. Pickard, R. J. Needs, *Phys. Rev. B.* **2015**, *91*, 214104.
[31] D. Ge, V. Domnich, Y. Gogotsi, *J. Appl. Phys.* **2004**, *95*, 2725.
[32] S. Mannepalli, K. S. R. N. Mangalampalli, *J. Appl. Phys.* **2019**, *125*, 225105.
[33] S. Ruffell, J. E. Bradby, J. S. Williams, *Appl. Phys. Lett.* **2007**, *90*, 131901.
[34] S. Ruffell, B. Haberl, S. Koenig, J. E. Bradby, J. S. Williams, *J. Appl. Phys.* **2009**, *105*, 093513.
[35] B. Haberl, M. Guthrie, S. V. Sinogeikin, G. Shen, J. S. Williams, J. E. Bradby, *High Pressure Res.* **2015**, *35*, 99.
[36] G. Weill, J. L. Mansot, G. Sagon, C. Carlone, J. M. Besson, *Semicond. Sci. Technol.* **1989**, *4*, 280.
[37] I. Zarudi, L. C. Zhang, W. C. D. Cheong, T. X. Yu, *Acta Mater.* **2005**, *53*, 4795.
[38] J. Hay, W. Olive, A. Bolshakov, G. Pharr, *MRS Online Proc. Libr.* **1998**, *522*, 101.
[39] G. J. Schaffar, D. Tscharnuter, P. J. Imrich, V. MaierKiener. *Thin Solid Films* **2024**, *80*, 140597.

[40] A. Leitner, V. Maier-Kiener, D. Kiener, *Mater. Des.* **2018**, *146*, 69.

[41] S. R. Kalidindi, S. Pathak, *Acta Mater.* **2008**, *56*, 3523.

[42] S. Pathak, S. R. Kalidindi, *Mater. Sci. Eng.: R: Rep.* **2015**, *91*, 1.

[43] L. A. Smillie, M. Niihori, L. Rapp, B. Haberl, J. S. Williams, J. E. Bradby, C. J. Pickard, A. V. Rode, *Phys. Rev. Mater.* **2020**, *4*, 093803.

[44] R. J. Kobliska, S. A. Solin, M. Selders, R. K. Chang, R. Alben, M. F. Thorpe, D. Weaire, *Phys. Rev. Lett.* **1972**, *29*, 725.

[45] M. Hanfland, K. Syassen, *High Pressure Res.* **1990**, *3*, 242.

[46] H. Olijnyk, A. P. Jephcoat, *Phys. Status Solidi* **1999**, *211*, 413.

[47] A. Kailer, K. G. Nickel, Y. G. Gogotsi, *J. Raman Spectrosc.* **1999**, *30*, 939.

[48] H. I. T. Hauge, M. A. Verheijen, S. Conesa-Boj, T. Etzelstorfer, M. Watzinger, D. Kriegner, I. Zardo, C. Fasolato, F. Capitani, P. Postorino, S. Kölling, A. Li, S. Assali, J. Stangl, E. P. A. M. Bakkers, *Nano Lett.* **2015**, *15*, 5855.

[49] Y. B. Gerbig, C. A. Michaels, J. E. Bradby, B. Haberl, R. F. Cook, *Phys. Rev. B* **2015**, *92*, 214110.

[50] I. Zarudi, J. Zou, L. C. Zhang, *Appl. Phys. Lett.* **2003**, *82*, 874.

[51] J. Crain, G. J. Ackland, J. R. Maclean, R. O. Piltz, P. D. Hatton, G. S. Pawley, *Phys. Rev. B* **1994**, *50*, 13043.

[52] R. O. Piltz, J. R. Maclean, S. J. Clark, G. J. Ackland, P. D. Hatton, J. Crain, *Phys. Rev. B* **1995**, *52*, 4072.

[53] S. Wippermann, Y. He, M. Vörös, G. Galli, *Appl. Phys. Rev.* **2016**, *3*, 040807.

[54] B. Haberl, T. A. Strobel, J. E. Bradby, *Appl. Phys. Rev.* **2016**, *3*, 040808.

[55] A. P. Bartók, J. Kermode, N. Bernstein, G. Csányi, *Phys. Rev. X* **2018**, *8*, 041048.

[56] G. Ge, F. Rovaris, D. Lanzoni, L. Barbisan, X. Tang, L. Miglio, A. Marzegalli, E. Scalise, F. Montalenti, *Acta Mater.* **2024**, *263*, 119465.

[57] F. Rovaris, A. Marzegalli, F. Montalenti, E. Scalise, *Mater. Today Nano* **2025**, *29*, 100548.

[58] J. C. Jamieson, *Science* **1963**, *139*, 762.

[59] M. I. Mcmahon, R. J. Nelmes, *Phys. Rev. B* **1993**, *47*, 8337.

[60] M. I. Mcmahon, R. J. Nelmes, N. G. Wright, D. R. Allan, *Phys. Rev. B* **1994**, *50*, 739.

[61] H. Olijnyk, S. K. Sikka, W. B. Holzapfel, *Phys. Lett. A* **1984**, *103*, 137.

[62] S. L. Butler, J. F. Partridge, X. Huang, I. Suarez-Martinez, N. A. Marks, J. E. Bradby, D. G. Mcculloch, *Appl. Phys. Lett.* **2023**, *123*, 231903.

[63] D. Kiener, M. Wurmshuber, M. Alfreider, G. J. K. Schaffar, V. Maier-Kiener, *Curr. Opin. Solid State Mater. Sci.* **2023**, *27*, 101108.

[64] C. Lin, X. Liu, D. Yang, X. Li, J. Smith, B. Wang, H. Dong, S. Li, W. Yang, J. Tse, *Phys. Rev. Lett.* **2020**, *125*, 155702.

[65] V. Domnich, Y. Gogotsi, *Rev. Adv. Mater. Sci.* **2002**, *3*, 1.

[66] G. J. K. Schaffar, J. Kappacher, D. Tscharnuter, V. Maier-Kiener, *JOM* **2022**, *74*, 2220.

[67] T. Juliano, V. Domnich, Y. Gogotsi, *J. Mater. Res.* **2004**, *19*, 3099.

[68] A. P. Thompson, H. M. Aktulga, R. Berger, D. S. Bolintineanu, W. M. Brown, P. S. Crozier, P. J. In 'T Veld, A. Kohlmeyer, S. G. Moore, T. D. Nguyen, R. Shan, M. J. Stevens, J. Tranchida, C. Trott, S. J. Plimpton, *Comput. Phys. Commun.* **2022**, *271*, 108171.

[69] A. Stukowski, *Modell. Simul. Mater. Sci. Eng.* **2010**, *18*, 015012.

[70] P. Giannozzi, O. Baseggio, P. Bonfà, D. Brunato, R. Car, I. Carnimeo, C. Cavazzoni, S. De Gironcoli, P. Delugas, F. Ferrari Ruffino, A. Ferretti, N. Marzari, I. Timrov, A. Urru, S. Baroni, *J. Chem. Phys.* **2020**, *152*, 154105.

[71] J. P. Perdew, K. Burke, M. Ernzerhof, *Phys. Rev. Lett.* **1996**, *77*, 3865.

[72] W. Kohn, L. J. Sham, *Phys. Rev.* **1965**, *140*, A1133.

[73] J. Sun, A. Ruzsinszky, J. Perdew, *Phys. Rev. Lett.* **2015**, *115*, 036402.

[74] Y. Yao, Y. Kanai, *J. Chem. Phys.* **2017**, *146*, 224105.

[75] S. Lehtola, C. Steigemann, M. J. T. Oliveira, M. A. L. Marques, *SoftwareX* **2018**, *7*, 1.

[76] J. P. Perdew, A. Ruzsinszky, G. I. Csonka, O. A. Vydrov, G. E. Scuseria, L. A. Constantin, X. Zhou, K. Burke, *Phys. Rev. Lett.* **2008**, *100*, 136406.

[77] D. R. Hamann, *Phys. Rev. B* **2013**, *88*, 085117.

[78] M. J. Van Setten, M. Giantomassi, E. Bousquet, M. J. Verstraete, D. R. Hamann, X. Gonze, G.-M. Rignanese, *Comput. Phys. Commun.* **2018**, *226*, 39.

[79] H. J. Monkhorst, J. D. Pack, *Phys. Rev. B* **1976**, *13*, 5188.

[80] S. Baroni, S. De Gironcoli, A. Dal Corso, P. Giannozzi, *Rev. Modern Phys.* **2001**, *73*, 515.

[81] N. T. Hung, J. Huang, Y. Tatsumi, T. Yang, R. Saito, *Comput. Phys. Commun.* **2024**, *295*, 108967.

[82] I. Timrov, N. Vast, R. Gebauer, S. Baroni, *Phys. Rev. B* **2013**, *88*, 064301.

[83] I. Timrov, N. Vast, R. Gebauer, S. Baroni, *Comput. Phys. Commun.* **2015**, *196*, 460.

[84] D. Rocca, R. Gebauer, Y. Saad, S. Baroni, *J. Chem. Phys.* **2008**, *128*, 154105.

[85] P. Vinet, J. H. Rose, J. Ferrante, J. R. Smith, *J. Phys.: Condens. Matter* **1989**, *1*, 1941.

[86] E. S. Toberer, A. Zevalkink, G. J. Snyder, *J. Mater. Chem.* **2011**, *21*, 15843.

[87] S. Wong, B. Haberl, B. Johnson, A. Mujica, M. Guthrie, J. Mccallum, J. Williams, J. Bradby, *Phys. Rev. Lett.* **2019**, *122*, 105701.

[88] B. C. Johnson, B. Haberl, J. E. Bradby, J. C. Mccallum, J. S. Williams, *Phys. Rev. B* **2011**, *83*, 235205.